Ceramics International 49 (2023) 22529–22536

Contents lists available at ScienceDirect

Ceramics International

journal homepage: www.elsevier.com/locate/ceramint

3D printing of cubic zirconia lattice supports for hydrogen production

Irene Díaz-Herrezuelo [a], Martin Koller [b], Asuncion Quintanilla [c], Gonzalo Vega [c], Jose A. Casas [c], Domingo Pérez-Coll [a], Hanus Seiner [b], M. Isabel Osendi [a], Pilar Miranzo [a], Manuel Belmonte [a,*]

[a] Institute of Ceramics and Glass (ICV, CSIC), Kelsen 5, 28049, Madrid, Spain
[b] Institute of Thermomechanics, Czech Academy of Sciences, Dolejškova 5, 18200, Prague, Czech Republic
[c] Chemical Engineering Department, Universidad Autónoma de Madrid, 28049, Madrid, Spain

ARTICLE INFO

Handling Editor: Dr P. Vincenzini

Keywords:
3D printing
Zirconia
Ceramic supports
Catalysts
Hydrogen production

ABSTRACT

The demand for hydrogen has extraordinarily grown during the last years, being one of the most attractive forms of fuels to produce green energy. Cubic zirconia ceramics are considered promising catalytic supports, and the additive manufacturing of porous 3D structures based on these ceramics could enhance their catalytic performance. Herein, lightweight highly porous (up to 88%) 3D patterned 8 mol% yttria-stabilized cubic zirconia (8YSZ) scaffolds are manufactured by robocasting from pseudoplastic aqueous-based inks to produce catalytic supports for the hydrogen (H_2) production. These scaffolds are thermally treated at temperatures ranging between 1000 and 1400 °C and, hence, mechanically and electrically characterized. 3D 8YSZ structures sintered at 1200 °C, with an appropriate balance between high porosity (86%) and compressive strength (3.7 MPa), are impregnated with palladium (Pd) catalytic nanoparticles and employed in the catalytic dehydrogenation of renewable formic acid (FA) using a fixed-bed reactor. 3D Pd/8YSZ catalyst leads to the continuous production of CO-free H_2 with a FA conversion of 32% at T = 55 °C.

1. Introduction

8 mol% yttria-stabilized cubic zirconia (8YSZ) ceramics are extensively employed as electrolytes (also as 8YSZ-based composite electrodes) in solid oxide fuel cells (SOFC) [1] and gas sensors [2] due to their oxygen-ion conductivity, which is associated to a great surface oxygen vacancy concentration and selective bulk oxygen mobility. Besides, 8YSZ ceramics have also been explored as support in heterogeneous catalysis for oxidation reactions, such as oxidation, hydrogenation, amination or isomerization [3], mainly using platinum catalytic nanoparticles supported on the 8YSZ powders. In all these kinds of applications, the additive manufacturing (AM) of cellular membranes, electrodes or supports would promote the increment in the mass transfer and accessibility to catalytic active sites in catalytic supports [4], or would reduce the internal resistance of SOFC [5].

In the last years, the development of 3D patterned porous ceramic scaffolds with high degree of accuracy has experienced a great advance by using AM technologies [6]. In particular, direct ink writing (DIW), also known as robocasting, stands out because it is a fast, versatile and inexpensive AM technique that enables building scaffolds with geometric and material complexities, without composition limitations, from concentrated aqueous colloidal inks with low organics contents [7]. In the case of zirconia ceramics, most of the works in the AM field have been focused on the development of complex dense parts [8], and just few investigations have reported the AM by robocasting of highly porous 3D patterned zirconia architectures [9–13]. In most of these studies, researchers employed aqueous inks with solid contents ranging from 28 to 50 vol% and different dispersant/binder/plasticizer organic systems. The majority of the 3D printed structures were produced from tetragonal zirconia phase powders -commonly 3 mol% yttria-stabilized zirconia (3YSZ) and, to a lesser extent, 12 mol% ceria-stabilized zirconia (CEZ-12) [13]-, which seems more appropriate for orthopaedic and bone tissue engineering applications than the cubic phase because of the better mechanical properties of the resulting material. At present, to the best of our knowledge, only the work of Peng et al. [11] has described the building of cellular cubic zirconia (6YSZ) scaffolds. In this case, inks with a shear thinning behaviour containing 38 vol% of 6YSZ plus an organic additive system based on polyvinyl alcohol, polyethylene glycol, L-ascorbic acid and citric acid, were prepared to print hexagonal and rectangular thin mesh structures, which were sintered at temperatures ranging from 1450 to 1700 °C for 20 h. However, information related to the porosity, mechanical strength or any other property of the scaffolds

* Corresponding author.
E-mail address: mbelmonte@icv.csic.es (M. Belmonte).

https://doi.org/10.1016/j.ceramint.2023.04.087
Received 28 February 2023; Received in revised form 28 March 2023; Accepted 11 April 2023
Available online 11 April 2023

was not provided. In addition to this work, two investigations reported the development of 8YSZ [14] and lanthanum strontium manganite (LSM)/8YSZ [15] inks (~50 vol% of solids loading) for robocasting non-patterned specimens, in particular, 3D printed bulk plates and electrodes, respectively, for use as solid oxide cells, although the rheological properties of the inks were not described.

On the other hand, the demand of hydrogen has extraordinarily grown during the last years [16], being one of the most attractive forms of fuels to produce green energy. In this way, the continuous hydrogen production from the catalytic decomposition of formic acid (FA) is of great interest as FA is a bio-renewable liquid organic hydrogen carrier [17]. Therefore, the aim of the present work is to manufacture, for the first time, highly porous 3D patterned robocast 8YSZ scaffolds, which are impregnated with palladium (Pd) nanoparticles catalyst to preliminary investigate their catalytic performance in the hydrogen production from FA. This approach is highly innovative as this kind of reaction using catalysts supported on 3D printed ceramic structures has not been reported hitherto. The 8YSZ scaffolds were robocast from pseudoplastic aqueous inks, which were rheologically characterized. The as-printed scaffolds were sintered at distinct temperatures to find an appropriate balance between high porosity, necessary to anchor the Pd nanoparticles to the ceramic filaments after the impregnation step, and adequate compressive strength of the 3D structures to be handled and support the demanding conditions of the catalytic fixed-bed reactor. The heat treated 8YSZ supports were fully characterized, including the analysis of their compressive strengths and ionic conductivities.

2. Experimental

2.1. Manufacturing of 8YSZ scaffolds

Aqueous printable ceramic inks were prepared by mixing and homogenising YSZ powders (TZ-8YS, Tosoh Co., mean particle size of 0.5 μm), ultrapure water and a set of organics, including dispersants and viscosifiers, in a planetary centrifugal mixer (ARE-250, Thinky Co.) that contained silicon nitride balls. The following organics were employed: high-molecular polyethylenimine (H-PEI, PEI 25000, <1 wt% of water content, Sigma Aldrich), low-molecular polyethylenimine (L-PEI, PEI 2000, 50 wt% of water content, Sigma Aldrich), methylcellulose (MC, Methocel F4M, 95 wt% of water content, Dow Chemical Co.), and ammonium polyacrylate (APA, Darvan 821A, 60 wt% of water content, Vanderbilt Minerals, LCC). While both H-PEI and L-PEI were selected as dispersants, MC acted as viscosifier and APA promoted the ink flocculation and, as anionic polyelectrolyte, balanced the charges coming from PEI. The different components forming the ink were sequentially added in ten steps, and after each step the ink was homogenized in the mixer at 1600 rpm for 30 s.

The rheological properties of the ink, in particular, the apparent viscosity (η) as a function of the shear rate ($\dot{\gamma}$), and the shear storage (G′) and loss (G″) moduli versus the shear stress (τ) were measured at 25 °C using a rheometer (CVO 100 D, Bohlin Instruments) with a cone-and-plate geometry (diameter: 40 mm; cone angle: 4°). In order to determine the viscosity, the angular velocity of the cone varied from 0.01 to 100 s^{-1}; whereas the moduli were calculated using the oscillation mode (frequency of 1 Hz) and ascending stress sweeps from 0.5 to 1000 Pa.

Unframed logpile type cylindrical scaffolds of 16.3 mm in diameter and 5.3 mm in height were computer designed (CAD, RoboCAD 4.2, 3-D Inks LLC) using the following parameters: 20 stacked layers, orthogonal pattern of filaments, rod spacing in each layer of 1.33 mm, and z-spacing of 0.26 mm. Afterwards, the scaffolds were printed in air onto flat alumina substrates with a three-axis robocasting system (A-3200, 3-D Inks LLC), nozzle tips with an inner diameter of 330 μm (Precision Tips; Nordson EFD Inc.), and a x-y table velocity of 10 mm s^{-1}. The as-printed 3D 8YSZ structures were first heat treated in air at 600 °C for 2 h employing heating/cooling rates of ~3 °C·min^{-1} to remove the organics employed to formulate the ceramic ink [18]. Then, the scaffolds were sintered in air in a chamber furnace with $MoSi_2$ heating elements (Thermolyne 46100, ThermoFisher Scientific) at temperatures (T_s) ranging from 1000 to 1400 °C using heating/cooling rates of ~10 °C·min^{-1} and a holding time at the maximum temperature of 2 h.

Geometrical (ρ_{geo}) and bulk densities (ρ_{bulk}), the latter linked to the zirconia skeleton of the scaffold, were assessed from their weight and dimensions, and by the Archimedes' method, respectively. Total porosity (π_{total}) was obtained from ρ_{geo} and the theoretical density of 8YSZ (6.0 g cm^{-3}). 3D porosity (π_{3D}), associated to the open channels designed by CAD, was calculated from π_{total}, the porosity of the rods (estimated from ρ_{bulk}) and the volume fraction of rods in the whole structure [19]. The 3D structures were microstructurally characterized by X-ray diffraction (XRD, Bruker D5000, Siemens), optical stereomicroscopy (SMZ1000, Nikon) and field emission scanning electron microscopy (FESEM, S-4700, Hitachi).

The compressive strength (σ_c) of the scaffolds (13.8 mm in diameter and 4.2 mm in height) as a function of T_s was determined using a universal testing machine with a load cell of 5 kN (ZwickiLine Z5.0 TS, Zwick-Roell) and a constant displacement rate of 0.5 mm min^{-1}. The scaffolds were firstly gently ground at the top/bottom surfaces (patterned-sides) to homogeneously distribute the load on the whole structure. Average data for each T_s corresponded to a minimum of five compression tested scaffolds.

The electrical behaviour of the scaffolds was studied by impedance spectroscopy using a potentiostat/galvanostat equipment integrated with a frequency-response-analyser module (Autolab PGSTAT302N-FRA2, Metrohm). Platinum electrodes were deposited over the circular surfaces of the scaffolds by means of a Pt ink (Metalor) and sintered at 950 °C for 1 h. The experimental procedure was performed in the temperature range of 250–950 °C with an applied signal amplitude of 50 mV and a frequency range of 10^{-1}-10^{6} Hz. Total resistances of the scaffolds were extracted from the impedance spectra by accounting for contributions of the bulk and grain boundary processes. In order to get a better understanding of the transport process in the scaffolds, impedance spectra were compared with those obtained on a pressed and densified cylindrical 8YSZ pellet sintered at 1500 °C. These conditions were selected to get a fully densified sample to get good accuracy for the determination of the ionic conductivity of 8YSZ in bulk, which will be employed as reference value.

2.2. Development of 3D Pd/8YSZ monoliths and catalytic performance

Pd nanoparticles were immobilized on the surface of 8YSZ scaffolds sintered at 1200 °C because these 3D structures exhibited a good balance between their porosity and compressive strength to be used as potential catalytic support, as it will be explained in the next sections. In brief, 8YSZ scaffolds were first stirred for 1 h into 45 mL of 1.62 M $(NH_4)_2SO_4$ solution with oscillating mixer with rollers (RollerMixD, Ovan). Then, they were dried at 95 °C for 3 h and calcined in air at 500 °C during 3 h [20]. Pd nanoparticles were synthesized by means of a deposition-precipitation process on these SO_4^{2-} doped 8YSZ scaffolds, adapting the methodology reported by Kim et al. [21]. In essence, doped 8YSZ monoliths were immersed and stirred for 1 h in 75 mL of 2.7 mM Na_2CO_3 solution and, afterwards, 4 mL of as-prepared Na_2PdCl_4 solution (0.47 M) were added to the solution, stirred for 1 h and heated at 95 °C to evaporate water and achieve the complete deposition of Pd^{2+} on the monoliths. These scaffolds were heated in air at 300 °C during 3 h and, hence, Pd^{2+} ions were reduced to metal Pd by a dropwise addition of 10 ml of $NaBH_4$ (4.7 mM). Finally, the resulting 3D Pd/8YSZ catalytic monoliths were washed with distilled water and dried overnight at 60 °C. These monoliths were tested in the continuous production of hydrogen from FA through a dehydrogenation reaction.

FESEM with coupled energy dispersive X-ray (EDX) detector and transmission electron microscope operating at 200 kV (TEM, JEOL 2100F) were employed to analyse 3D Pd/8YSZ scaffolds before ("fresh") and after ("used") the catalytic reaction. The Pd content in the monoliths

was measured by total reflection X-ray fluorescence (TXRF) using a benchtop S2 PICOFOX TXRF spectrometer (Bruker Nano). The exposed Pd surface species (Pd^{0}, $Pd^{\delta+}$) were quantified by X-ray photoelectron spectroscopy (XPS). The spectra measurements were performed with the PHI5000 VersaProbe II using a monochromatic Al-Ka X-ray beam (1486.6 eV). Charge referencing was measured against adventitious carbon (C 1s at 284.8 eV).

The FA decomposition reaction was conducted in a fixed-bed reactor operated in continuous mode. Five 3D Pd/8YSZ monolith pieces (catalyst weight, $W_{CAT} \sim 4$ g) were settled in a double jacket glass tube (GE Healthcare, XK16/20 mm) between two beds of spherical glass beads of 2 mm diameter. Water, as heating fluid, was recirculated in the double jacket to assure the desired reaction temperature inside the reactor, T = 55 °C. The FA solution ($C_{FA,0}$ = 1 M) was preheated and fed to the bottom of the reactor at a liquid flow rate (Q_L) = 0.25 mL min^{-1} by a piston pump (Shimadzu LC-20AD). Thus, the reactor was operated at the spatial time (τ) = $W \cdot Q_L^{-1}$ = 267 $g_{CAT} \cdot h \cdot L^{-1}$. Helium (He) was used as carrier gas with a flow rate (Q_G) = 17 NmL·min^{-1} to ensure a continuous flow of gas. The liquid and gas from the reactor effluent was continuously separated and cooled down in a Peltier cell and, then, collected and analysed. Gas samples were collected using gas sampling bags (Supelco). The evolution of gas composition during the reaction was studied by a gas chromatograph (Agilent 6890) equipped with a thermal conductivity detector employing a Varian select permanent gases/CO_2 column, and using He as carrier gas on the analysis. H_2, CO, CO_2, O_2 and N_2 gases were calibrated employing three commercial standards. On the other hand, FA concentration (C_{FA}) in the liquid effluent was measured by spectrophotometry at the wavelength of 210 nm in a Cary 60 Vis-UV spectrophotometer.

The FA conversion (X_{FA}) was calculated as follows:

$$X_{FA}(\%) = \frac{C_{FA,0} - C_{FA}}{C_{FA,0}} \cdot 100 \quad (1)$$

According to the reaction stoichiometry: $HCOOH \rightarrow H_2 + CO_2$, the molar flow of H_2 (F_{H2} in mol·min^{-1}) can be determined as:

$$F_{H2} = F_{FA,0} \cdot X_{FA} = Q_L \cdot C_{FA,0} \cdot X_{FA} \quad (2)$$

and, therefore, the H_2 flow rate (Q_{H2}, in mL·min^{-1}) produced was:

$$Q_{H2} = \frac{F_{H2}\, R\, T}{P} \quad (3)$$

where R is the ideal gas constant (0.082 atm L K^{-1}·mol^{-1}), T the reaction temperature in K and P the atmospheric pressure in atm. The CO_2 gas flow rate was calculated considering the composition ratio of H_2 and CO_2 measured in the gas chromatograph:

$$Q_{CO_2} = \frac{Q_{H_2}}{\text{molar ratio } H_2/CO_2} \quad (4)$$

Finally, the evolved gas flow rate (Q_{gas}) was the sum of the H_2 and CO_2 flow rates.

3. Results and discussion

3.1. 8YSZ scaffolds

Fig. 1 shows the rheological behaviour of the printable ceramic ink, which contained 78.5 wt% of 8YSZ, 16.9 wt% of water (total content including the water from the organics), and 4.6 wt% of organics (2.7% H-PEI, 1.4% L-PEI, 0.1% MC, 0.4% APA), that corresponded to 38.2, 49.2 and 12.6 in vol%, respectively. As it can be seen, η linearly decreased with $\dot{\gamma}$ in about two orders of magnitude for the tested shear rate interval (Fig. 1a), confirming the pseudoplastic response of the ink that would allow continuously printing 8YSZ filaments through the nozzle tip with high stiffness. Besides, G′ of the ink (Fig. 1b) reached three times higher steady data (~1.5×10^5 Pa) than those measured for G'' (~4.5×10^4 Pa) until both curves crossed at a yield stress (τ_y) value of ~380 Pa, which would predict the assembling of robust scaffoldings. In fact, the as-printed (AP) architectures, formed by filaments perfectly reproducing the patterned structure of the CAD model, did not show any sign of damage and exhibited mechanical robustness (Fig. 2). The printable ink was attained after a progressive refinement of the ink composition by varying the solids/water/organics content and measuring their rheological properties (see some examples in Fig. S1); where an excess of organics content led to a slight decrease in G' (~3×10^4 Pa), G'' (~1×10^4 Pa) and τ_y (~175 Pa) as compared to the values attained for the selected ink.

The 3D structures and the filaments retained their shape after the sintering treatments, despite a considerable shrinkage of the scaffold took place with T_s (Fig. 2a), with reductions in the diameter and height from 16.2 to 5.0 mm (1000 °C) to 12.6 and 4.0 mm (1400 °C), respectively. Fig. 2b–d illustrates, as example, some images of a scaffold sintered at 1200 °C where the shape of the open channels and filaments was preserved.

XRD tests confirmed that all sintered 8YSZ scaffolds kept the cubic zirconia phase of the pristine powders (see Fig. S2 in the Supplementary Information). Table 1 collects the densities and porosities of the 8YSZ scaffolds versus T_s. As expected, an increment in T_s led to higher densities, although this effect was more pronounced at 1400 °C with an increase of ~80% for the ρ_{geo} (1.50 g cm^{-3}) and ρ_{bulk} (5.18 g cm^{-3}) as compared to the 1200 °C data, being that increment just ~ 20% when T_s raised from 1000 to 1200 °C. On the other hand, the total porosity slightly decreased (up to 13%) with T_s and the scaffolds reached π_{total} values from 88.1% (1000 °C) to 75.0% (1400 °C). The main contribution to the total porosity comes from the patterned structure, i.e. π_{3D}, which varied from 80.8 to 71.6% for the lower and higher T_s, respectively, although the effect of T_s is mostly reflected in the porosity of the ceramic skeleton (π_{rod}). In this way, 8YSZ filaments were significantly more porous at 1000 °C (60.9%) and 1200 °C (53.4%) than at 1400 °C (13.7%). FESEM observations evidenced the lack of rod densification at $T_s \leq 1200$ °C, with a microstructure formed by spherical-like grains of about 200 nm of diameter with low connectivity (Fig. 2e); whereas at

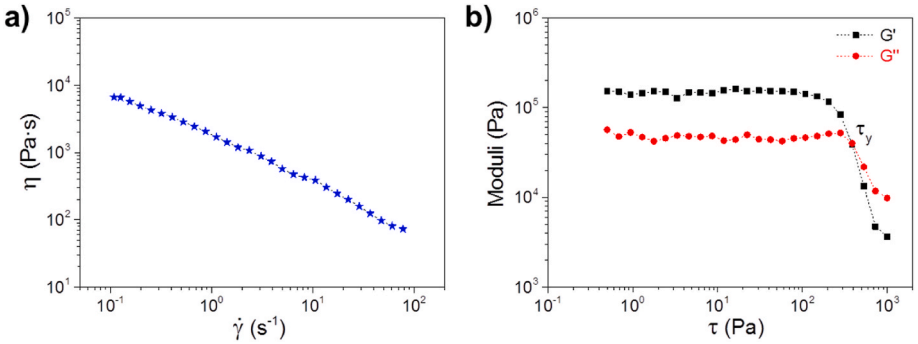

Fig. 1. a) Apparent viscosity (η) versus shear rate ($\dot{\gamma}$) and b) shear storage (G′) and loss (G″) moduli versus shear stress (τ) of the 8YSZ ink.

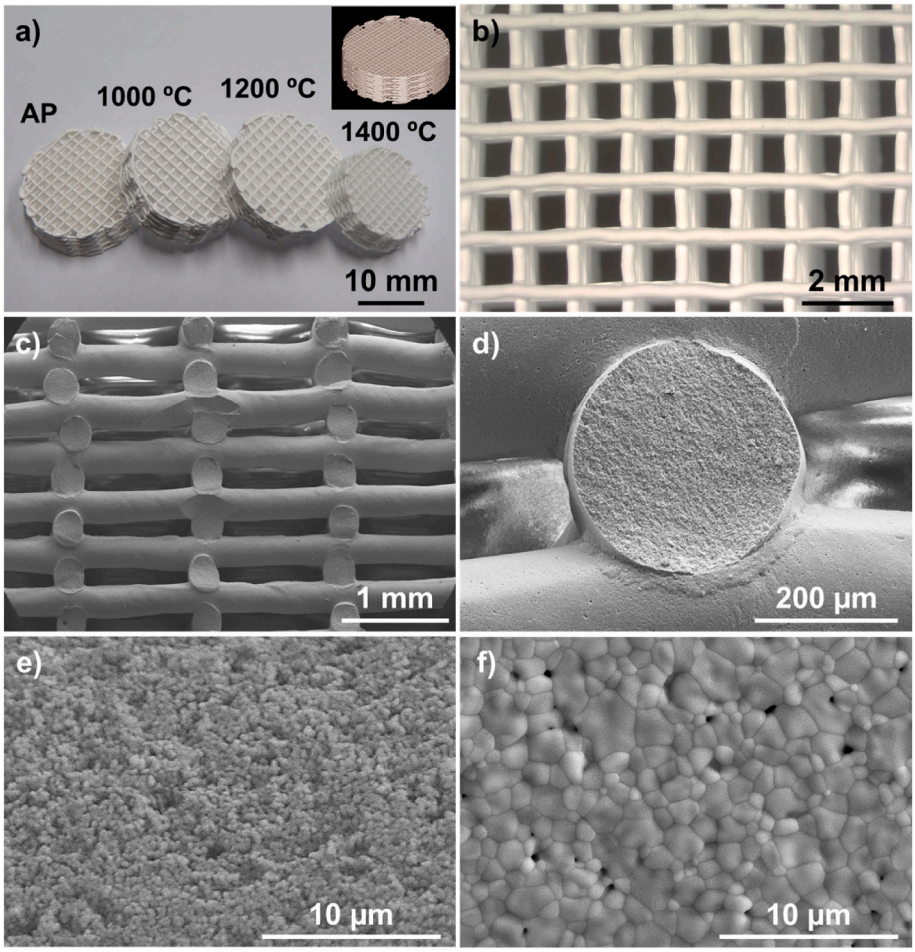

Fig. 2. a) Set of 8YSZ scaffolds heat treated at different temperatures. The inset corresponds to the CAD model. b) Optical image of the 8YSZ-1200 scaffold exhibiting the open channels and the filaments of the patterned structure. FESEM micrographs of the cross-section view of a fractured 3D 8YSZ-1200 showing the printed stacked layers (c), a detail of one rod (d). FESEM images of the microstructure at the surface of rods sintered at 1000 °C (e) and 1400 °C (f).

Table 1
Geometrical density (ρ_{geo}), bulk density (ρ_{bulk}), total porosity (π_{total}), 3D porosity (π_{3D}) and rod porosity (π_{rod}) of the scaffolds versus the sintering temperature (T_s).

T_s (°C)	ρ_{geo} (g·cm^{-3})	ρ_{bulk} (g·cm^{-3})	π_{total} (%)	π_{3D} (%)	π_{rod} (%)
1000	0.72 ± 0.03	2.34 ± 0.17	88.1 ± 0.5	80.8 ± 0.8	60.9 ± 2.8
1200	0.84 ± 0.02	2.80 ± 0.11	85.9 ± 0.3	78.4 ± 0.5	53.4 ± 1.8
1400	1.50 ± 0.04	5.18 ± 0.28	75.0 ± 0.7	71.6 ± 1.4	13.7 ± 4.7

1400 °C the densification of the rods occurred and the microstructure was composed of equiaxial grains that grown up to 1–2 µm of average size (Fig. 2f). Therefore, it is possible to tailor the porosity and microstructure of the 3D cellular structures, which will have an impact on their final properties and potential applications. Besides, an appropriate balance between porosity and mechanical resistance should be reached.

The mechanical performance under compression test of 8YSZ scaffolds is collected in Fig. 3. Stress-strain curves (Fig. 3a) evidenced a distinct response with the sintering temperature. All scaffolds showed an elastic region at the beginning of the test and, as T_s increased, the curves exhibited a larger number of saw-tooth like events that corresponded to the failure of discrete filaments forming the scaffolding, although the 3D architectures still survived until the maximum compressive strength (crushing, σ_c) was reached. At low T_s, saw-tooth like events were not observed as σ_c was quickly reached. As tests progressed the scaffolds gradually collapsed. Fig. 3b plots the average σ_c values versus π_{total} of 3D 8YSZ structures, evidencing that σ_c decreased as the total porosity augmented, following a similar trend than that observed in cellular materials [22]. 8YSZ-1000 scaffolds attained a σ_c value of 0.6 ± 0.1 MPa, with a strain at the maximum stress of 2.7 ± 0.9%, which reflects their high porosity (~88%). Although they are enough robust to be manipulated, the mechanical resistance is insufficient for demanding applications such those required, for instance, in catalytic reactors. In the case of 8YSZ-1200 scaffolds, the strength increased in five times as compared to 8YSZ-1000, with σ_c = 3.7 ± 0.3 MPa and strain of 4.1 ± 0.8%, keeping at the same time a high π_{total} value (~86%). This response would allow using these scaffolds in catalytic reactions where a good balance between porosity, to access to the active sites, and mechanical resistance is necessary. Finally, 8YSZ-1400 reached the highest strength value (σ_c = 6.9 ± 1.1 MPa, strain of 5.2 ± 1.3%, π_{total} = 75%) that corresponded to an increment of one order of magnitude and ~90% as compared to the specimens sintered at 1000 and 1200 °C, respectively. These scaffolds sintered at 1400 °C presented low porosity of the skeleton (π_{rod} ~ 14%) and high mechanical resistance, which would allow using them in high-temperature electrochemical devices and in the new micro-energy conversion systems. Despite mechanical data for 3D cellular 8YSZ scaffolds have not been previously reported, compressive strength results can be found for robocast 3YSZ scaffolds. In this way, Li et al. [9] obtained σ_c values of 8–10 MPa for scaffolds with 63–55% of porosity; while Peng et al. [11] reported σ_c = 57 MPa for 3D mesh

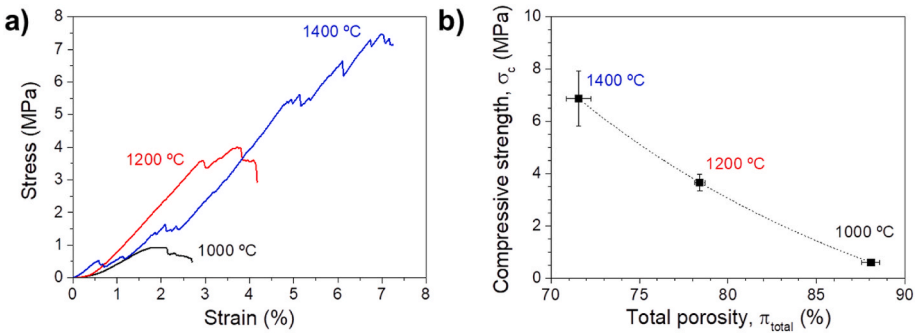

Fig. 3. a) Representative examples of the stress-strain curves and b) average compressive strength (σ_c) values versus the total porosity (π_{total}) for 8YSZ scaffolds sintered at distinct temperatures (1000–1400 °C).

structures with 49% of macroporosity using three-point bending tests. Gaddam et al. [12] recently reached a value of 70 MPa for scaffolds containing 69% of porosity, which was attributed by the authors to the high solid content of the ink (48 vol%). Finally, Tabard et al. [13], employing tetragonal CEZ-12 powders, obtained robocast scaffolds with strengths ranging from 9.9 MPa, for the structure containing 64% of total porosity, to 0.4–0.2 MPa, for the scaffolds with the highest porosities (80–83%). In the former case, σ_c value would fit to the trend shown in Fig. 3b; whereas highly porous specimens would deviate from that tendency probably due to the large microporosity of the ceramic filaments promoted by the addition of sacrificial fugitives. It is important to mention that, in general, tetragonal zirconia materials present better mechanical properties than cubic zirconia ones due to transformation toughening effects, which highlights the relevance of the values attained for 3D 8YSZ. Comparing with other highly porous (>70%) robocast ceramic scaffolds, current data for 3D 8YSZ are within the range of those attained for 3D structures based on, among others, hydroxyapatite [23], geopolymer [24], SiC [25] or γ-Al_2O_3 [26]. Nevertheless, an important issue when different studies are compared is the patterned structure and cell geometry as, for instance, the presence or lack of external frame, a higher or lower ratio between the rod spacing in each layer and the rod diameter, or different cell orientation would modify the mechanical resistance of the scaffolds despite they present similar total porosities.

The comparison of the electrical behaviour of scaffolds and the fully dense pellet provided suitable information regarding the role played by the macro-porosity on the connectivity of the whole 3D structures. Besides, a great difference in the apparent electrical behaviour between the scaffolds and the pellet was observed, as Fig. S3 shows with some examples of their experimental impedance spectra. Arrhenius representations of the apparent conductivity (σ_{app}) for the sintered scaffolds and the dense pellets in the range 250–950 °C are plotted in Fig. 4a. The higher σ_{app} for the pellets, as compared with the scaffolds, is ascribed to a more accurate determination of the real volume for electrical transport. The values for the scaffolds were obtained by normalisation with the area (A) and thickness (L) comprised by the external structure (cylinder), which is expected to produce a clear underestimation of the true conductivity values, given that only a fraction of the circular area of the cylinder participates in the conduction process. To make a more accurate comparison of the real conduction process of the different structures, an estimation of the conduction area for the scaffolds was done, considering that the transport occurred through the contacted rods that cross the structure (Fig. 2b and c). Fig. 4b and Table 2 showed that the obtained values of conductivity of the scaffolds were improved by one order of magnitude after normalisation with the contacted area

Table 2
Ionic conductivity of different samples, including the values obtained with the external surfaces of the structures (σ_{app}) and the values considering the contacted area of rods crossing the scaffolds (σ_N). For the pellet, both magnitudes are identical.

Sample	Testing temperature (°C)	σ_{app} (S·m^{-1})	σ_N (S·m^{-1})
Scaffold 1200 °C	900	0.17	1.49
	800	7.3×10^{-2}	0.65
	700	2.5×10^{-2}	0.22
	500	1.0×10^{-3}	8.6×10^{-3}
Scaffold 1400 °C	900	1.04	10.54
	800	0.54	5.51
	700	0.23	2.34
	500	0.01	0.13
Dense Pellet	900	15.21	15.21
	800	7.72	7.72
	700	3.08	3.08
	500	0.16	0.16

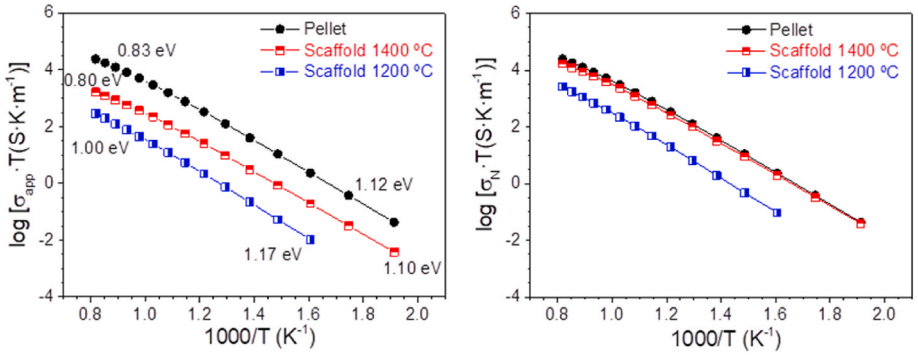

Fig. 4. Arrhenius representation of the ionic conductivity for the scaffolds sintered at 1200 and 1400 °C and the dense pellet. a) Apparent total conductivity (σ_{app}) determined by the external dimensions of the structures and b) corrected σ_N for the scaffolds considering the conducting area through the contacted rods that cross the 3D structure.

for conduction (σ_N). The results evidenced that the scaffold sintered at 1400 °C presented values of ionic conductivity (σ_N = 0.13–10.54 S m^{-1}) only slightly lower than those obtained for the dense pellet (σ_N = 0.16–15.21 S m^{-1}), which is a clear indication that despite the scaffold still contains certain porosity, there is a very good contact between the rods crossing the structure in the current flow direction through the scaffold. On the other hand, the scaffold sintered at 1200 °C still presented values of conductivity considerably lower than those obtained for the other structures. This is a consequence of the very high porosity of this sample (Table 1), as it has been widely demonstrated for ceramic ionic conductors [27–29]. In this regard, the porosity led to a decrease in the true cross-sectional area of transport and an extension of the real conduction pathway, which were reflected in the increment of the resultant electrical resistance. Note that the minor differences observed in Fig. 4b for the pellet and the scaffold sintered at 1400 °C were also a consequence of different densification in both samples. In spite of this, the ionic conductivity at 800 °C of this 3D structure (~5.5 S m^{-1}) is within the values required for practical applications as electrolyte membrane for SOFC [30], being quite similar to values recently reported for 8YSZ membranes additive manufactured by stereolithography (~4 S m^{-1}) considering their effective area [31].

3.2. Pd/8YSZ monoliths and catalytic performance

Fig. 5a shows a black coloured fresh 3D Pd/8YSZ catalyst due to the presence of metallic Pd, in contrast with the white 8YSZ-1200 scaffold. In fact, Pd^0 and Pd^{2+} species were identified by XPS in the former scaffolds, with a Pd^{2+}:Pd^0 atomic ratio of 0.14 (Fig. 5b). Both species are required to activate the catalytic reaction [21,32–35]. TXRF and FESEM-EDX analysis confirmed that the Pd content on the monolith was 5 wt%. Besides, TEM observations allowed estimating, by using ImageJ software, an average size of the Pd nanoparticles of 5.2 ± 1.2 nm (Fig. 5c), which were homogenously distributed on the scaffold surface, as elemental mapping by EDX confirmed (Fig. S4).

The results obtained in the H_2 production from FA decomposition over 3D Pd/8YSZ catalysts are provided in Fig. 6. As can be observed, the initial FA conversion was 32% and the evolved gas flow rate produced 4.2 mL min^{-1} at the selected operating conditions: T = 55 °C,

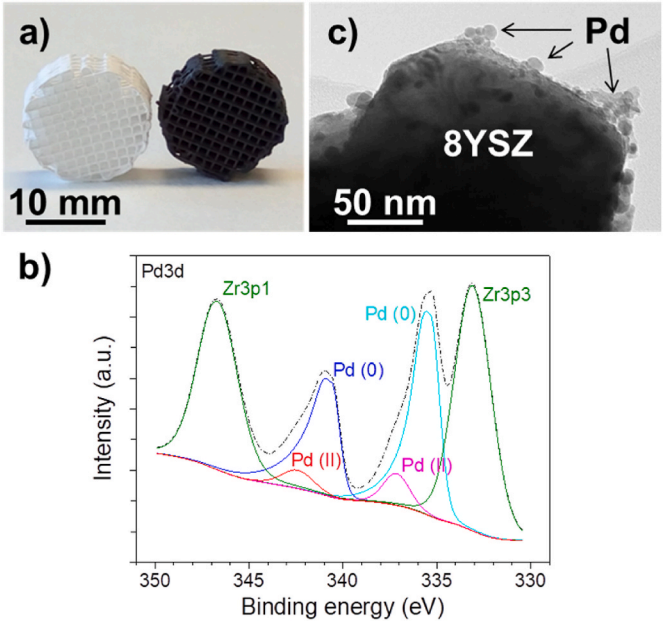

Fig. 5. a) Comparison between 3D 8YSZ-1200 scaffold (left) and fresh 3D Pd/8YSZ catalysts (right), b) XPS spectrum of Pd core level for fresh 3D Pd/8YSZ catalyst and c) TEM micrograph showing some Pd nanoparticles on the surface of 8YSZ particles for the fresh 3D Pd/8YSZ catalyst.

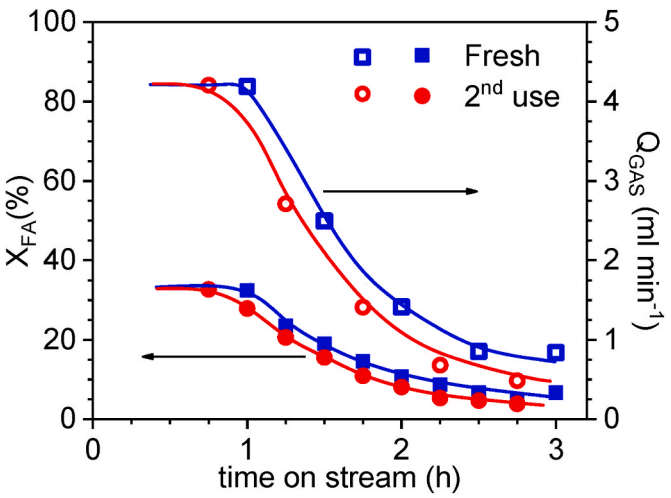

Fig. 6. Results of the catalytic performance of 3D Pd/8YSZ catalysts for the continuous production of hydrogen from FA decomposition. FA conversion (X_{FA}) and gas flow rate (Q_{gas}) as a function of the time on stream using the following operating conditions: $C_{FA,0}$ = 1 M, Q_L = 0.25 mL min^{-1}, W_{CAT} = 4 g, T = 55 °C and P = 1 atm.

$C_{FA,0}$ = 1 M and τ = 267 g_{CAT}·h·L^{-1}. This activity is low compared with that exhibited by the extensively studied carbon-supported Pd catalysts in powder form, as expected since the latter have a higher surface area than the structured catalysts. For instance, Caiti et al. [36] reported FA conversions above 80% in a fixed bed reactor using 5 wt% Pd/activated carbon catalyst powders, with a Pd particle size of 3.2 nm, at T = 50 °C, $C_{FA,0}$ = 0.5 M and τ = 10 g_{CAT}·h·L^{-1}. However, the present activity results are better than those attained with a ternary catalyst such as PtRuBiOx/C [37], which provided FA conversions of 5% in a fixed bed reactor operated at T = 60 °C, $C_{FA,0}$ = 1 M and τ = 3.3 g_{CAT}·h·L^{-1}. In any case, the practical value of this catalyst comes from its conformation as a robust structured catalyst, which is a requirement for its use at industrial scale. A catalyst in powdered form cannot be used at industrial scale due to the high pressure drop if it is packed in a fixed bed reactor or due to its possible blow out when used in fluidized-bed reactor. For this reason, catalysts always need to be shaped for industrial use, and the sufficient mechanical strength of the catalyst support is essential for the catalyst's long-term structural durability. To the best of our knowledge, this is the first work reporting the liquid organic hydrogen carrier technology for H_2 production using a structured reactor.

H_2 and CO_2 were the unique species detected in the evolved gas, with

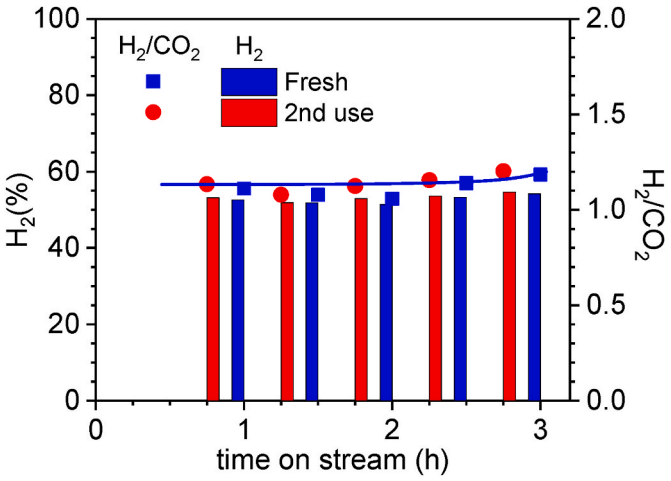

Fig. 7. H_2 molar percentage and H_2/CO_2 molar ratio in the evolved gas produced in the FA decomposition reaction upon 3D Pd/8YSZ catalysts.

a H_2/CO_2 molar ratio slightly above 1 (*viz.* 1.2) (Fig. 7), which can be due to their different solubility in the reaction media, as it was already observed in previous studies [34,38]. These results indicate that FA decomposition followed the desired route, i.e., the catalytic dehydrogenation to produce H_2 and CO_2; while the FA dehydration reaction did not take place. This last reaction produces CO as final product, species not detected in the gas effluent over the 3D Pd/8YSZ catalysts, and one of the species responsible for the Pd catalysts deactivation [39]. The catalytic activity of the 3D Pd/8YSZ catalysts progressively decreased from 1 h of operation, and they appeared completely deactivated after 3 h on stream (Fig. 6). This deactivation is unavoidable in Pd catalysts [35] and it occurs faster in continuous operation [36,37]. Herein, the major cause of deactivation is the fouling of the Pd active site by species of the reaction media, such as water and FA (or $HCOO^-$ species), both with similar boiling points, since the activity is restored after the drying of the catalyst at 60 °C overnight, see the 2nd use curve in Fig. 6. However, the deactivation began slightly earlier, as it was demonstrated by the lower gas flow rate (Q_{gas}) produced at a given time on stream compared to the fresh catalyst. The Pd^{2+}:Pd^{0+} atomic ratio remained unaltered (the XPS spectrum is shown in Fig. S5) and also the Pd particle size, now 5.9 ± 0.9 nm (Fig. S6). This means that other aspects must be considered to understand the slow irreversible deterioration upon use, such as the slight loss of Pd loading in the 3D catalysts, from 5.0 to 4.5 wt % according to the TXRF analysis.

It can be concluded that 3D Pd/8YSZ catalysts are promising candidates for the continuous production of CO-free H_2 using (renewable) FA as carrier. Though the manufacturing of the 3D Pd/8YSZ catalyst is not fully optimized, the use of a structured catalyst for the continuous production of hydrogen from FA has been unprecedentedly demonstrated, which encourages continuing the development of 3D Pd catalysts adapted to this increasingly demanded reaction. In addition, despite the ionic conductivity of 8YSZ does not seem to provide any specific benefit to this particular catalytic reaction, these 3D 8YSZ ceramic scaffolds could be tentatively explored in other processes where oxygen ions play an important role, such as in catalytic advanced oxidation reactions.

4. Conclusions

Unframed cylindrical cellular 8YSZ scaffolds were additive manufactured by robocasting from pseudoplastic aqueous inks (38 vol% of solids loading) that exhibited a yield stress of 380 Pa. The sintering at distinct temperatures (1000–1400 °C) of the as-printed patterned structures allowed developing lightweight 3D ceramic scaffolds with total porosity from 88 to 75%, rod porosity from 61 to 14%, 8YSZ grain size from 20 nm to 2 μm, and compressive strength from 0.6 to 6.9 MPa, which can be controlled depending on their final applications, as discussed in the present work for two of them. 8YSZ scaffolds behaved as ionic conductors when sintered at 1400 °C, with conductivity values at 800 °C of ~5 S m^{-1} that would be suitable for electrolyte membranes. Highly porous 3D printed structures sintered at 1200 °C were homogenously coated by Pd nanoparticles to produce 3D Pd/8YSZ catalysts, which acted as promising candidates for the continuous production of CO-free H_2 through the catalytic dehydrogenation of renewable FA. Pd^0 and Pd^{2+} species led to a FA conversion of 32% in a fixed-bed reactor operated in continuous mode, being the first time that a structured reactor based on 3D catalysts was employed for this kind of dehydrogenation reaction.

Declaration of competing interest

The authors declare that they have no known competing financial interests or personal relationships that could have appeared to influence the work reported in this paper.

Acknowledgements

This work was supported by the Spanish Government through RTI2018-095052-B-I00, PID2019-105079RB-I00 (MICINN/AEI/FEDER, UE), PID2021-125427OB-I00 (MICINN/AEI/FEDER, UE) and EIN2020-112153 (MCINN/AEI/10.13039/501100011033) projects, the latter also supported by the European Union through "NextGenerationEU/PRTR". M. Koller gratefully acknowledges funding within "Support for International Mobility of Researchers of the Institute of Thermomechanics, Czech Academy of Sciences, part II", no. CZ.02.2.69/0.0/0.0/18_053/0017555 of the Ministry of Education, Youth and Sports of the Czech Republic funded from the European Structure and Investment Funds (ESIF). G. Vega acknowledges the Universidad Autónoma de Madrid for the Predoctoral contract. The authors thank J. Mejía for her permanent technical assistance in the catalytic experiments.

Appendix A. Supplementary data

Supplementary data to this article can be found online at https://doi.org/10.1016/j.ceramint.2023.04.087.

References

[1] N. Mahato, A. Banerjee, A. Gupta, S. Omar, K. Balania, Progress in material selection for solid oxide fuel cell technology: a review, Prog. Mater. Sci. 72 (2015) 141–337, https://doi.org/10.1016/j.pmatsci.2015.01.001.
[2] N. Miura, T. Sato, S.A. Anggraini, H. Ikeda, S. Zhuiykov, A review of mixed-potential type zirconia-based gas sensors, Ionics 20 (2014) 901–925, https://doi.org/10.1007/s11581-014-1140-1.
[3] M.N. Tsampas, F.M. Sapountzi, P. Vernoux, Applications of yttria stabilized zirconia (YSZ) in catalysis, Catal. Sci. Technol. 5 (2015) 4884–4900, https://doi.org/10.1039/C5CY00739A.
[4] S. Lawson, X. Li, H. Thakkar, A.A. Rownaghi, F. Rezaei, Recent advances in 3D printing of structured materials for adsorption and catalysis applications, Chem. Rev. 121 (2021) 6246–6291, https://doi.org/10.1021/acs.chemrev.1c00060.
[5] A. Pesce, A. Hornés, M. Núñez, A. Morata, M. Torrell, A. Tarancón, 3D printing the next generation of enhanced solid oxide fuel and electrolysis cells, J. Mater. Chem. 8 (2020), 16926, https://doi.org/10.1039/D0TA02803G.
[6] F. Zhang, Z. Li, M. Xu, S. Wang, N. Li, J. Yang, A review of 3D printed porous ceramics, J. Eur. Ceram. Soc. 42 (2022) 3351–3373, https://doi.org/10.1016/j.jeurceramsoc.2022.02.039.
[7] E. Peng, D. Zhang, J. Ding, Ceramic robocasting: recent achievements, potential, and future developments, Adv. Mater. 30 (2018), 1802404, https://doi.org/10.1002/adma.201802404.
[8] X. Zhang, X. Wu, J. Shi, Additive manufacturing of zirconia ceramics: a state-of-the-art review, J. Mater. Res. Technol. 9 (2020) 9029–9048, https://doi.org/10.1016/j.jmrt.2020.05.131.
[9] Y.-Y. Li, L.-T. Li, B. Li, Direct write printing of three-dimensional ZrO_2 biological scaffolds, Mater. Des. 72 (2015) 16–20, https://doi.org/10.1016/j.matdes.2015.02.018.
[10] J. Liao, H. Chen, H. Luo, X. Wang, K. Zhou, D. Zhang, Direct ink writing of zirconia three-dimensional structures, J. Mater. Chem. C 5 (2017) 5867–5871, https://doi.org/10.1039/C7TC01545C.
[11] E. Peng, X. Wei, U. Garbe, D. Yu, B. Edouard, A. Liu, J. Ding, Robocasting of dense yttria-stabilized zirconia structures, J. Mater. Sci. 53 (2018) 247–273, https://doi.org/10.1007/s10853-017-1491-x.
[12] A. Gaddam, D.S. Brazete, A.S. Neto, B. Nan, J.M.F. Ferreira, Three-dimensional printing of zirconia scaffolds for load bearing applications: study of the optimal fabrication conditions, J. Am. Ceram. Soc. 104 (2021) 368–4380, https://doi.org/10.1111/jace.17874.
[13] L. Tabard, V. Garnier, E. Prud'Homme, E.-J. Courtial, S. Meille, J. Adrien, Y. Jorand, L. Gremillard, Robocasting of highly porous ceramics scaffolds with hierarchized porosity, Addit. Manuf. 38 (2021), 101776, https://doi.org/10.1016/j.addma.2020.101776.
[14] A. Ghazanfari, W. Li, M.C. Lea, J.L. Watts, G.E. Hilmas, Additive manufacturing and mechanical characterization of high density fully stabilized zirconia, Ceram. Int. 43 (2017) 6082–6088, https://doi.org/10.1016/j.ceramint.2017.01.154.
[15] S. Anelli, M. Rosa, F. Baiutti, M. Torrell, V. Esposito, A. Tarancón, Hybrid-3D printing of symmetric solid oxide cells by inkjet printing and robocasting, Addit. Manuf. 51 (2022), 102636, https://doi.org/10.1016/j.addma.2022.102636.
[16] E.B. Agyekum, C. Nutakor, A.M. Agwa, S.A. Kamel, A critical review of renewable hydrogen production methods: factors affecting their scale-up and its role in future energy generation, Membranes 12 (2022) 173, https://doi.org/10.3390/membranes12020173.
[17] Q.-L. Zhu, Q. Xu, Liquid organic and inorganic chemical hydrides for high-capacity hydrogen storage, Energy Environ. Sci. 8 (2015) 478–512, https://doi.org/10.1039/C4EE03690E.
[18] A.D. Salazar-Aguilar, A. Quintanilla, S.M. Vega-Díaz, J.A. Casas, P. Miranzo, M. I. Osendi, M. Belmonte, Iron-based metal-organic frameworks integrated into 3D

printed ceramic architectures, Open Ceram 5 (2021), 100047, https://doi.org/10.1016/j.oceram.2020.100047.
[19] A.D. Salazar-Aguilar, A. Quintanilla, P. Lopez, C. Martinez, S.M. Vega-Díaz, J. A. Casas, P. Miranzo, M.I. Osendi, M. Belmonte, 3D printed Fe/γ-Al_2O_3 monoliths from MOF-based boehmite inks for the catalytic hydroxylation of phenol, ACS Appl. Mater. Interfaces 14 (2022) 920–932, https://doi.org/10.1021/acsami.1c19755.
[20] S. Melada, R. Rioda, F. Menegazzo, F. Pinna, G. Strukul, Direct synthesis of hydrogen peroxide on zirconia-supported catalysts under mild conditions, J. Catal. 239 (2006) 422–430, https://doi.org/10.1016/j.jcat.2006.02.014.
[21] Y. Kim, D.H. Kim, Understanding the effect of Pd size on formic acid dehydrogenation via size-controlled Pd/C catalyst prepared by $NaBH_4$ treatment, Appl. Catal. B Environ. 244 (2019) 684–693, https://doi.org/10.1016/j.apcatb.2018.12.008.
[22] L.J. Gibson, M.F. Ashby, Cellular Solids: Structure and Properties, Cambridge University Press, Cambridge, 1999.
[23] J. Roleceka, L. Pejchalová, F.J. Martínez-Vázquez, P. Miranda, D. Salamon, Bioceramic scaffolds fabrication: indirect 3D printing combined with ice-templating vs. robocasting, J. Eur. Ceram. Soc. 39 (2019) 1595–1602, https://doi.org/10.1016/j.jeurceramsoc.2018.12.006.
[24] G. Franchin, P. Scanferla, L. Zeffiro, H. Elsayed, A. Baliello, G. Giacomello, M. Pasetto, P. Colombo, Direct ink writing of geopolymeric inks, J. Eur. Ceram. Soc. 37 (2017) 2481–2489, https://doi.org/10.1016/j.jeurceramsoc.2017.01.030.
[25] A. Gomez-Gomez, J.J. Moyano, B. Roman-Manso, M. Belmonte, P. Miranzo, M. I. Osendi, Highly-porous hierarchical SiC structures obtained by filament printing and partial sintering, J. Eur. Ceram. Soc. 39 (2019) 688–695, https://doi.org/10.1016/j.jeurceramsoc.2018.12.034.
[26] L. Moreno-Sanabria, C. Ramírez, M.I. Osendi, M. Belmonte, P. Miranzo, Enhanced thermal and mechanical properties of 3D printed highly porous structures based on γ-Al_2O_3 by adding graphene nanoplatelets, Adv. Mater. Technol. (2022), 2101455, https://doi.org/10.1002/admt.202101455.
[27] S.P.S. Badwal, J. Drennan, Yttria-zirconia: effect of microstructure on conductivity, J. Mater. Sci. 22 (1987) 3231–3239, https://doi.org/10.1007/BF01161187.
[28] M.C. Steil, F. Thevenot, M. Kleitz, Densification of yttria-stabilized zirconia: impedance spectroscopy analysis, J. Electrochem. Soc. 144 (1997) 390, https://doi.org/10.1149/1.1837416.
[29] D. Pérez-Coll, E. Sánchez-López, G.C. Mather, Influence of porosity on the bulk and grain-boundary electrical properties of Gd-doped ceria, Solid State Ionics 181 (2010) 1033–1042, https://doi.org/10.1016/j.ssi.2010.06.006.
[30] J.W. Fergus, Electrolytes for solid oxide fuel cells, J. Power Sources 162 (2006) 30–40, https://doi.org/10.1016/j.jpowsour.2006.06.062.
[31] K. Jia, L. Zheng, W. Liu, J. Zhang, F. Yu, X. Meng, C. Li, J. Sunarso, N. Yang, A new and simple way to prepare monolithic solid oxide fuel cell stack by stereolithography 3D printing technology using 8 mol% yttria stabilized zirconia photocurable slurry, J. Eur. Ceram. Soc. 42 (2022) 4275–4285, https://doi.org/10.1016/j.jeurceramsoc.2022.03.060.
[32] J. Li, W. Chen, H. Zhao, X. Zheng, L. Wu, H. Pan, J. Lu, Y. Chen, J. Lu, Size-dependent catalytic activity over carbon-supported palladium nanoparticles in dehydrogenation of formic acid, J. Catal. 352 (2017) 371–381, https://doi.org/10.1016/j.jcat.2017.06.007.
[33] H.J. Jeon, Y.M. Chung, Hydrogen production from formic acid dehydrogenation over Pd/C catalyst: effect of metal and support properties on the catalytic performance, Appl. Catal. B Environ. 210 (2017) 212–222, https://doi.org/10.1016/j.apcatb.2017.03.070.
[34] F. Sánchez, D. Motta, A. Roldan, C. Hammond, A. Villa, N. Dimitratos, Hydrogen generation from additive-free formic acid decomposition under mild conditions by Pd/C: experimental and DFT studies, Top. Catal. 61 (2018) 254–266, https://doi.org/10.1007/s11244-018-0894-5.
[35] C. Martin, A. Quintanilla, G. Vega, J.A. Casas, Formic acid-to-hydrogen on Pd/AC catalysts: kinetic study with catalytic deactivation, Appl. Catal. B Environ. 317 (2022), 121802, https://doi.org/10.1016/j.apcatb.2022.121802.
[36] M. Caiti, D. Padovan, C. Hammond, Continuous production of hydrogen from formic acid decomposition over heterogeneous nanoparticle catalysts: from batch to continuous flow, ACS Catal. 9 (2019) 9188–9198, https://doi.org/10.1021/acscatal.9b01977.
[37] C. Hu, S. Ting, J. Tsui, K. Chan, Formic acid dehydrogenation over PtRuBiOx/C catalyst for generation of CO-free hydrogen in a continuous-flow reactor, Int. J. Hydrogen Energy 37 (2012) 6372–6380, https://doi.org/10.1016/j.ijhydene.2012.01.062.
[38] C. Hu, J.K. Pulleri, S. W Ting, K.Y. Chan, Activity of Pd/C for hydrogen generation in aqueous formic acid solution, Int. J. Hydrogen Energy 39 (2014) 381–390, https://doi.org/10.1016/j.ijhydene.2013.10.067.
[39] Q. Lv, Q. Meng, W. Liu, N. Sun, K. Jiang, L. Ma, Z. Peng, W. Cai, C. Liu, J. Ge, L. Liu, W. Xing, Pd-PdO Interface as active site for HCOOH selective dehydrogenation at ambient conditions, J. Phys. Chem. C 122 (2018) 2081–2088, https://doi.org/10.1021/acs.jpcc.7b08105.